Estimating the Height of CMEs Associated with a Major SEP Event
at the Onset of the Metric Type II Radio Burst during Solar Cycles 23 and 24

P. Mäkelä[1,2], N. Gopalswamy[2], S. Akiyama[1,2], H. Xie[1,2] and S. Yashiro[1,2]

[1]The Catholic University of America, Washington, DC 20064

pertti.makela@nasa.gov

[2]Nasa Goddard Space Flight Center, Greenbelt, MD 20771

To appear in Astrophysical Journal

ABSTRACT

We studied the coronal mass ejection (CME) height at the onset of 59 metric type II radio bursts associated with major solar energetic particle (SEP) events, excluding ground level enhancements (GLEs), during solar cycles 23 and 24. We calculated CME heights using a simple flare-onset method used by Gopalswamy et al. (2012b) to estimate CME heights at the metric type II onset for cycle-23 GLEs. We found the mean CME height for non-GLE events (1.72 $R_\odot$) to be $\sim$12% greater than that (1.53 $R_\odot$) for cycle-23 GLEs. The difference could be caused by more impulsive acceleration of the GLE-associated CMEs. For cycle-24 non-GLE events, we compared the CME heights obtained using the flare-onset method and the 3-D spherical-shock fitting method and found the correlation to be good (CC=0.68). We found the mean CME height for cycle 23 non-GLE events (1.79 $R_\odot$) to be greater than for cycle 24 non-GLE events (1.58 $R_\odot$), but statistical tests do not definitely reject the possibility of coincidence. We suggest that the lower formation height of the shocks during cycle 24 indicates a change in the Alfvén speed profile because solar magnetic fields are weaker and plasma density levels are closer to the surface than usual during cycle 24. We also found that complex type III bursts showing diminution of type III emission in the 7–14 MHz frequency range are more likely associated with events with the CME height at the type II onset above 2 $R_\odot$, supporting suggestions that the CME/shock structure causes the feature.

Subject headings: shock waves — Sun: corona — Sun: coronal mass ejections (CMEs) — Sun: radio radiation

1. Introduction

Type II radio bursts occurring at metric wavelengths are known to be associated with coronal shocks (e.g., Wild & McCready 1950; Uchida 1960; Nelson & Melrose 1985). The type II radio bursts are identified as slowly drifting features in radio dynamic spectra. The frequency of type II emission decreases as the shock propagates away from the Sun because the plasma density decreases as a function of the radial distance. However, the temporal evolution and frequency characteristics of metric type II bursts can be quite complex due to variation of the plasma density in the low corona. The exact nature of the drivers of metric type II producing shocks, i.e. are they flare blast waves or bow shocks ahead of a coronal mass ejection (CME), has been debated (e.g., Gopalswamy 2006; Vršnak & Cliver 2008), but it is generally accepted that type II radio burst are caused by beams of shock-accelerated electrons that excite Langmuir waves that are converted into radio waves at the fundamental and second harmonic of the local electron plasma frequency (e.g., Nelson & Melrose 1985). Recently Schmidt & Cairns (2014) have demonstrated an excellent agreement between observed type II bursts and the results of their magnetohydrodynamic simulations that incorporate a realistic 3-D CME model with an analytic kinetic radiation theory of type II emission. Their results give support to the interpretation adopted here that CME-driven shocks produce type II bursts. Because radio emission does not propagate along magnetic field lines unlike the solar energetic particles (SEPs), the onset of a metric type II burst anywhere on the visible solar disk can be readily observed. Therefore, metric type II bursts are suitable for analyzing the height of shock formation and the onset of particle acceleration by shocks in the corona.

Solar eruptions with a type II radio burst are associated with other radio bursts like type III radio bursts. The drift rates of type III bursts are much higher than those of type II bursts. Type III radio bursts are caused by beams of electrons propagating along

interplanetary magnetic field lines. Type III producing electrons are accelerated in flares, i.e., in the region of the magnetic field reconnection close to the solar surface. A special subgroup of type III bursts known as complex type III bursts is known to be connected with SEP events (Cane et al. 2002; MacDowall et al. 2003). However, Gopalswamy & Mäkelä (2010) analyzed a sequence of three complex type III bursts in April 2008 and found that only the two complex type III bursts accompanied by a type II burst did result in an SEP event. Gopalswamy et al. (2000) noted that all observed complex type III events are associated with type II radio bursts in their study of 25 radio-rich CMEs. Reiner & Kaiser (1999) analyzed complex type III bursts in the frequency range of 1–14 MHz. They found that all events typically showed reduced radio emission around 7 MHz, which corresponds to the height of 2.5 $R_\odot$ in the solar corona. They speculated that 7 MHz level corresponds to a disturbed coronal region which suppresses the propagating electron beam from emitting radiation because turbulence prevents the formation of a well-defined beam. Gopalswamy (2004) suggested that the existence of the diminution depends on the CME location with respect to the electron acceleration site and the observer, because of possible effects on the propagation of electrons or radio waves by the intervening CME.

In this study we estimate the height of the shock at the onset of the type II radio bursts. We assume that coronal shocks producing metric type II radio bursts are driven by CMEs. We calculate the CME height at the type II onset using a simple model that relies on the observational fact that the CME acceleration phase and the impulsive phase of the flare occur simultaneously (e.g., Zhang et al. 2001; Cliver et al. 2005). The CME height is estimated by assuming that the CME accelerates with a constant acceleration from rest to the projection-corrected CME speed (i.e., the space speed of the CME) between the onset and peak time of the associated flare as explained in Gopalswamy et al. (2012b). The assumed constancy of the CME acceleration is naturally a simplification. Recent studies suggest that the peak times of hard X-ray emission (HXR) of the flare and the CME

acceleration occur near simultaneously (e.g., Temmer et al. 2008; Berkepile-Stoiser et al. 2012). Gopalswamy et al. (2012b) used this flare-onset method to estimate the height of the CME at the onset of the metric type II burst for cycle-23 ground level enhancement (GLE) events. They found that the mean and median distances of the CME were 1.53 $R_\odot$ and 1.47 $R_\odot$, respectively. We expand their analysis to include all major non-GLE SEP events that occurred during November 1997–January 2014. We also compare the CME heights between the previous cycle 23 and the ongoing cycle 24.

For cycle 24 SEP events, we also estimate the shock formation height by fitting a spherical shock model to the extreme ultra-violet (EUV) and white-light images of the CME and compare the heights with the results of the flare-onset method. This 3-D spherical-shock fitting method differs from the wave-diameter method used by Gopalswamy et al. (2013), which uses only 2-D images taken from a single view point. We assume that the radial distance where the CME-driven shock forms corresponds to the height of the leading edge of the bright disturbance visible in the coronagraphic running difference images at the onset time of the type II radio bursts. Even though the shock propagates ahead of the CME, the distance between the shock nose and the driving CME is sufficiently small near the Sun. During some events, the shock sheath can be seen as a faint layer followed by the brighter driving CME (e.g., Sheeley et al. 2000; Vourlidas et al. 2003; Gopalswamy & Yashiro 2011). In these cases the location of the shock is measured as the leading edge of the sheath. There are some evidence that the radio source of a metric type II could be located at the flank region of the CME-driven shock (e.g., Claßen & Aurass 2002; Zucca et al. 2014), but here we use the height of the leading edge. In addition, we briefly discuss the correlation between the properties of complex type III radio bursts and the estimated CME height.

2. Event Selection

The initial data set consists of all major SEP events with a reported metric type II burst, excluding all GLE events, during the study period extending from November 1997 to January 2014 (see http://cdaw.gsfc.nasa.gov/CME_list/sepe/). We have followed the suggestion made by Thakur et al. (2014) and excluded the 2014 January 6 SEP event as a GLE event, even though there is some discussion whether or not this event fulfills the formal definition of a GLE event (e.g. Bazilevskaya et al. 2014). Major SEP events are defined as those with the peak proton intensity in the GOES > 10 MeV channel equals or exceeds 10 pfu (1 pfu = 1 particle sr^{-1} cm^{-2} s^{-1}). In principle, it is possible that our selected set of SEP events still includes GLE-like events because the detection of a GLE event depends on the observer's magnetic connection of the nose region (Gopalswamy et al. 2014b). However, GLE events are rare and hence the number of SEP events where the GeV-range particles remained undetected because the GOES spacecraft was not magnetically connected to the nose region of the shock is low.

From the list of major SEP events with a metric type II burst, we selected all those events for which adequate GOES data of the associated soft X-ray flare was available. We used GOES 1–8 Å X-ray profiles and the daily NOAA Solar Event Reports (Edited Events) (http://www.swpc.noaa.gov/ftpmenu/warehouse.html) to determine the magnitude and the onset and peak times of the associated GOES X-ray flare. Flare locations are taken from NOAA reports or determined from images of the Extreme ultraviolet Imaging Telescope (EIT Delaboudinière et al. 1995) on board the Solar and Heliospheric Observatory (SOHO). The associated CMEs were identified using the Large Angle and Spectrometric Coronagraph (LASCO; Brueckner et al. 1995) CME catalog (http://cdaw.gsfc.nasa.gov/CME_list/index.html) (Yashiro et al. 2004; Gopalswamy et al. 2009b). Our final data set consist of 59 SEP events listed in Table 1. The columns in Table

1 are: the type II date (1) and time (2), the first observation date (3) and time (4) of the associated CME, the CME space speed (5) and width (6), the location of the associated flare (7), the flare onset date (8) and time (9), the flare peak date (10) and time (11), the magnitude of the flare (12), the calculated constant acceleration of the CME (13) and the height of the CME (14) at the type II onset calculated using the flare-onset method. The last column (15) of Table 1 gives the measured height of the CME at the type II onset obtained by 3-D fitting a spherical shock model to CME images. The onset times of the metric type II bursts listed in Table 1 are the earliest reported times compiled from the NOAA Solar Event Reports, except the onset times of the 2000 June 6 and November 8 events that are from Gopalswamy (2003). Often different observatories report different onset times for the same metric type II burst, therefore by selecting the earliest onset times we guarantee that our estimation is the lowest CME height consistent with the radio observations. Some additional details of the entries in Table 1 are given in sections 3 and 5 discussing data analysis methods.

3. Flare-Onset Method for the CME Height Estimation

Because we cannot accurately measure the radial height of a CME if its propagation direction deviates considerably from the sky plane, other indirect methods to estimate the CME height have been suggested. Recently, Gopalswamy et al. (2012b) described four different methods, which they used to estimate the CME heights of cycle-23 GLE events. Here we use the flare-onset method where the CME is assumed to be launched at the flare onset time. The flare onset and peak times are compiled from the online NOAA solar event reports. Occasionally solar flares occur in a close sequence and hence their light curves will be overlapping in GOES X-ray measurements. In that case the onset time listed in the NOAA solar event report might correspond to a wrong flare. In order to verify the flare

onset times, we analyzed the logarithmic time derivatives of GOES soft X-ray flare light curves (see Fig. 1) and adjusted the flare onset time if necessary. The moment when the time derivative of the X-ray flux becomes positive is taken to be the new corrected onset time of the flare. This correction reduces the error in the flare timing, but the corrected onset time will be delayed relative to the true onset time because the flare onset is partially masked by another overlapping flare.

At the onset time of the flare, the CME is assumed to be launched from the height of 1.25 $R_\odot$. This initial height for the CME launch was chosen because it corresponds to the upper boundary of the cavity above the prominence (Gibson et al. 2006, 2010). The CME accelerates from rest to the final speed, which is reached at the flare peak time (see e.g., Zhang & Dere 2006). Hence the CME acceleration during the flare rise phase can be calculated as:

$$a = V_{CME}/(t_{FlarePeak} - t_{FlareOnset}), \tag{1}$$

where V_{CME} is the estimated space speed of the CME, and $t_{FlarePeak}$ and $t_{FlareOnset}$ are the flare peak and onset times, respectively. Previous studies have provided observational evidence for contemporaneity of the CME acceleration with the flare impulsive phase (e.g., Zhang et al. 2001). After the peak time of the flare, the CME propagates with a constant speed V_{CME}. In most cases the type II onset occurs during the acceleration phase of the CME. The CME space speed V_{CME} is estimated using a cone model for halo CMEs (Xie et al. 2004, see also the CDAW halo CME list http://cdaw.gsfc.nasa.gov/CME_list/halo/halo.html) and a geometrical projection correction for non-halo CMEs. The geometrical correction simply multiplies the measured sky plane speed by $1/\sin\theta$, where θ is the angular distance of the CME source from the solar disk center. The site of the associated flare is used as the location of the CME source region.

4.   Average CME Height at the Onset of Type II Burst

In Figure 2 we have plotted the estimated CME heights (column 14 in Table 1) for all 59 events as a function of type II onset time. The CME heights are estimated using the flare-onset method. The mean (1.72 $R_\odot$) and median (1.60 $R_\odot$) height for all events are marked in the upper right corner. The mean and median CME height for non-GLE SEP events are respectively ∼12% and ∼9% higher than the mean (1.53 $R_\odot$) and median (1.47 $R_\odot$) height for cycle-23 GLEs obtained by Gopalswamy et al. (2012b). GLE-associated CMEs on average are faster than CMEs associated with a non-GLE SEP event (e.g., Gopalswamy et al. 2010). Therefore, the more impulsive acceleration of GLE-associated CMEs could result in the lower shock formation height because the shock speed will exceed the ambient Alfvén speed sooner. The peak of CME acceleration coincides with the HXR peak of the associated flare, but the maximum speed of the CME is reached well after the HXR peak (Berkepile-Stoiser et al. 2012).

Gopalswamy et al. (2012b) estimated that the assumed initial CME height of 1.25 Rs could introduce a small error of 10% in the calculated CME heights. They estimated the error by assuming that in some events the initial CME height could be as low as 1.13 Rs (Gopalswamy et al. 2012a). If we use as the lower limit the more extreme value by Gallagher et al. (2003), who obtained a best fit to the EUV and white-light observations of the CME on 2002 April 21 with an initial CME height of 25±2 Mm (∼1.04 $R_\odot$), the estimated error in the CME heights becomes ∼17%.

The horizontal dashed lines in Fig. 2 indicate the mean CME height averaged over cycle 23 (1.79 $R_\odot$) and cycle 24 (1.58 $R_\odot$) CMEs, respectively. The respective median values were 1.61 $R_\odot$ and 1.45 $R_\odot$. For comparison, we have also plotted the CME heights at the type II onset for GLE events (red circles). Cycle-23 GLE events were analyzed by Gopalswamy et al. (2012b). For the GLE71 in the cycle 24 we calculated the CME height

at the type II onset using the flare-onset method and for the GLE72 we took the estimated value from Thakur et al. (2014). The significance of the difference between the mean CME heights on cycles 23 and 24 was estimated using the Student's t-test. The calculated p-values were 0.129 (equal variances) and 0.071 (unequal variances). Mann-Whitney U-test (Mann & Whitney 1947) for median values gave a p-value equal to 0.048. The U-test also assumes that variances of the two distributions are equal. Because the p-values are larger than or very close to the 95% confidence threshold of 0.05, we cannot definitely reject the null hypothesis that the mean or median values are equal. However, the result suggests that possibly the coronal conditions during cycles 23 and 24 are different.

5.   CME Height Estimation by Forward Fitting a Spherical Shock Model

In order to estimate the validity of the flare-onset method, we estimated the CME heights for 15 cycle-24 events by fitting a spherical shock model to near-simultaneous EUV and white-light running difference images of the CME provided by the Atmospheric Imaging Assembly (AIA; Lemen et al. 2012) on board the Solar Dynamic Observatory (SDO) and by COR1 and COR2 coronagraphs of the Sun Earth Connection Coronal and Heliospheric Investigation (SECCHI; Howard et al. 2008) on board the Solar TErrestrial RElations Observatory (STEREO). Images closest to the onset time of the metric type II burst from as many spacecraft as possible were used for the model fitting. The number of viewpoints used in fitting depends on the location of the eruption relative to the spacecraft at the time of the type II onset. For the 3-D spherical shock model fitting we used RTCLOUDWIDGET.PRO program available in the SolarSoft IDL library (http://www.lmsal.com/solarsoft/). The spheroidal shock model is defined by three parameters (see Fig. 3): the height h (the height of the spheroid from the solar center in unit of solar radii), the self-similarity coefficient κ ($b = (h-1)\kappa$), where b is the azimuthal semi-axis of the spheroid, and the eccentricity e.

We assume that shock fronts are spherical, i.e., we fix the eccentricity $e = 0$. In addition to the three parameters of the spherical model, we need to set the latitude and longitude of the CME source region, i.e., set the intersection point of the radial axis of the spherical model on the solar surface. The parameters are adjusted manually in order to achieve the best match for the wire-grid model of the shock front plotted over each CME image by the program. Because each near-simultaneous image shows the same CME imaged from a different viewpoint, the projection effects in the 3-D model fitting are significantly reduced.

Figure 4 shows the 15 events for which we were able to fit a spherical shock model. The deduced CME heights are listed in the column 15 of Table 1. The correlation between the flare-onset and spherical-shock methods is reasonably good, with the correlation coefficient CC=0.68. In calculating the correlation we have excluded four events, namely the 2012 July 19, 2012 August 31, 2012 September 27, and 2013 May 22 events. The four exclude outliers are marked by black filled circles in Fig. 4. We will discuss these events later in following section. The dashed line representing the linear fit between the estimated heights shows that the estimates from the flare-onset method are slightly lower than those of the spherical-shock method at the lower range of the CME heights where most of the events are clustered. The mean difference between the CME height estimates from the two methods for the 11 included events (blue circles in Fig. 4) is 0.20 $R_{\odot}$. Considering that the flare-onset method assumes a constant initial height and acceleration for the CME, obtained results are reasonably good.

6.   Starting Frequency of the Type II Burst

We can further evaluate the consistency of the CME height estimates plotted in Fig. 4 by using the radio observations of the associated type II burst. The starting frequency of the type II bursts depends on the height of the radio source: a higher starting frequency

indicates a radio source closer to the solar surface because the frequency of type II emission is proportional to the square root of the plasma density and the plasma density decreases as a function of the radial distance. Several models describing the density in the corona as a function of the radial distance have been suggested over the years (e.g., Saito et al. 1977; Leblanc et al. 1998). Because the density of the ambient plasma in the low corona varies from event to event, the radio frequency corresponding to a given coronal height varies accordingly. Generally, this density variation is accounted for by multiplying the density model by a factor that is obtained by matching the frequency calculated using the density model with the measured type II frequency at the time when we also have the measurement of the CME height available, usually based on a coronagraph image. In our study we cannot rely on CME height measurements, because we are interested in the validity of our CME height estimates. However, we still are able to make some conclusions based on the starting frequencies of the type II bursts.

In the NOAA reports, the measurement range of the most observatories reporting type II burst detections is limited to frequencies in the range 25–180 MHz. The reported maximum frequency most likely correspond harmonic emission. Only two or three of the type II bursts plotted in Fig. 4 did not have a clear fundamental-harmonic structure at metric wavelengths. Therefore, we divided the 15 data points plotted in Fig. 4 into two sets: those with the reported starting frequency between 160–180 MHz and those with the starting frequency (fs) below 160 MHz. For the six bursts with $fs < 160$ MHz the reported maximum frequencies were 120 MHz, 82 MHz, 100 MHz, 131 MHz, 60 MHz and 41 MHz. Assuming that harmonic emission was observed, $fs = 120$ MHz corresponds to the height of ∼1.25 $R_\odot$ according to the Saito density model (Saito et al. 1977). The height range of 2.0–2.5 $R_\odot$ correspond harmonic emission at frequencies 16 MHz–30 MHz. These numbers are only suggestive, because we do not know the exact density levels of the corona at the time of each type II burst. If the actual coronal densities are two times the Saito model

values then the corresponding radio frequency at a specific distance will be ∼1.41 higher.

In Figure 4 the events with the starting frequency below 160 MHz are marked by red circular rings. For all events except one that have the CME height measured using the spherical-shock method around or above 2 $R_\odot$, the type II starting frequency is below 160 MHz confirming that the radio source must have been at larger distances. Especially all excluded outliers (marked by black circles in Fig. 4) are among these events. This corroborates the results by the spherical-shock method. Correspondingly it also indicates that for some reason the flare-onset method must have underestimated the CME heights in the four excluded events. There is one event, the 2011 June 7 event, which have unexpectedly low starting frequency compared to the estimated height of the associated CME, ∼1.5 $R_\odot$. Next we look the details of the 2011 June 7 event.

6.1. The 2011 June 7 Event

The only exception among the events with the type II starting frequency below 160 MHz is the 2011 June 7 event. Various aspects of this filament eruption has been extensively analyzed (see e.g., Cheng et al. 2012; Dorovskyy et al. 2012; Innes et al. 2012; Li et al. 2012; Williams et al. 2012; Inglis & Gilbert 2013; van Driel-Gesztelyi et al. 2014). The metric type II was associated with a halo CME (HCME) at 06:49 UT that had an estimated space speed of 1321 km s^{-1}. The reported type II starting frequency for this event is 120 MHz, clearly suggesting that the CME height at the onset of the type II bursts should be similar to those of the four excluded events. The associated M2.5 flare at S21W54 started at 06:16 UT. However, both the flare-onset method and the spherical-shock method estimated the CME height to be ∼1.5 $R_\odot$. These estimates are in accordance with the estimated CME height by Cheng et al. (2012, their Fig. 2).

In Figure 5 we have plotted the onset of the radio burst reported by the Learmonth Solar Radio Spectrograph. The type II burst was reported to occur between 06:25–06:50 UT in the frequency range of 25–120 MHz, but have plotted a shorter time period to study the onset of the type II emission. A strong burst of radio emission is clearly observed below 120 MHz but this radio burst has a fractured structure with several narrow-band short-duration features showing varying drift slopes. These short-duration bursts could be due to flare-accelerated electrons propagating in the complex loop structures of the low corona. The highest-frequency feature around 120 MHz even appears to exhibit a reverse drift indicating electron beam propagating towards the Sun. There is a short-duration downward drifting feature starting around 42 MHz that resembles type II burst. However, this feature has a relatively high drift rate ($\sim$0.21 MHz/s), corresponding to a shock speed of $\sim$1800 km s^{-1}. This shock speed seems to be too fast, because the CME was still accelerating around 06:26 UT (see Cheng et al. 2012). In addition, the space speed of the CME was estimated to be 1321 km s^{-1} (CDAW HCME list), well below 1800 km s^{-1}. However, the CME probably was fast enough to drive a shock. The Wind/WAVES (Bougeret et al. 1995) observed decameter-to-kilometer range type II starting at $\sim$06:45 UT. Type II emission faded around $\sim$07:25 UT at $\sim$4 MHz and reappeared sporadically after $\sim$07:43 UT below 1 MHz. Based on the above considerations, we conclude that the decameter type II burst observed by Wind/WAVES could have been the extension of the metric type II burst but the exact onset time of the metric type II burst is uncertain. Dorovskyy et al. (2012) estimated that the type II onset times was 06:36 UT based on measurement by the UTR-2 and URAN-2 radio telescopes. This start time coincides with the estimated time of the CME speed maximum (Cheng et al. 2012). Further complication is that there are indications that the type II source was at first in the flank region and shifted later into the nose region of the shock (A. Bemporad, presentation at SCOSTEP's 13th Quadrennial Solar-Terrestrial Physics Symposium in Xi'An, China).

7. The Four Events with CME Height Discrepancies between Flare-Onset and Spherical-Shock Methods

The four events for which the flare-onset method gave significantly lower CME heights compared to the spherical-shock method were the 2012 July 19, 2012 August 31, 2012 September 27, and 2013 May 22 events. Next we describe briefly the details of these events and then summarize possible reasons for the CME height discrepancies.

The onset of the 2012 July 19 type II was reported by the Culgoora Solar Observatory radiospectrograph to be 05:24 UT at 100 MHz, but after inspecting the Culgoora dynamic spectra we shifted the onset one minute later to 05:25 UT. The Culgoora dynamic spectrum reveals relatively faint and short-duration (< 1 min) drifting features that look like type II emission. The radio burst was associated with a HCME observed at 05:24 UT by LASCO. The leading edge of the CME at that time was measured to be at the height of 2.67 $R_\odot$ (LASCO CME Catalog; http://cdaw.gsfc.nasa.gov/CME_list/index.html). This height is only slightly higher than our estimate of 2.48 $R_\odot$ from the spherical shock fit. The NOAA Solar Event report gives the onset of the M7.7 soft X-ray flare at 04:17 UT, but after inspecting the X-ray profile we revised the flare onset time to 05:07 UT due to overlapping flares. The flare occurred at S13W88 and it peaked at 05:58 UT. Because the CME occurred at the west limb of the Sun, the CME height measurements do not suffer from projection effects and therefore we take the space speed of the CME to be the speed given in the LASCO CME catalog, 1631 km s^{-1}. An intermittent DH type II was observed starting at 05:30 UT at the frequency of 5 MHz. The type III burst also becomes clearly more intense at the frequency of $\sim$5 MHz and below. A few much fainter and narrow type III emission lanes are visible starting around 9 MHz.

The HCME associated with the 2012 August 31 event was first observed at 20:00 UT with the space speed of 1442 km s^{-1}. The C8.4 flare at S19E42 was reported to start at

19:45 UT, which we corrected to 19:38 UT. Metric type II start time was 19:48 UT at the frequency of 120 MHz based on the dynamic spectra of Sagamore Hill Solar Radio Observatory of the Radio Solar Telescope Network (RSTN). The originally reported time at 19:42 UT was too early. The observed radio emission consists of sporadic but bright batches that suggest the existence of a metric type II radio burst. An intermittent DH type II burst was detected by Wind/WAVES and STB/WAVES between 20:00 UT and 23:45 UT in the frequency range of 0.4–16 MHz. As was the case during the 2012 July 19 event, an intensification of the type III emission was observed at the frequency of ∼6 MHz and below. Only two narrow and fainter type III bursts are visible above 6 MHz in the Wind/WAVES data.

The metric type II associated with the 2012 September 27 event was reported to start at 23:44 UT at the frequency of 60 MHz by Culgoora Solar Observatory. The metric type II burst was sporadic. The associated C3.7 flare occurred at 23:36 UT at N06W34. The first observation time of the associated CME was 00:12 UT on September 28. The CME space speed was estimated to be 1376 km s^{-1}. The WIND/WAVES and STEREO-B/WAVES instruments detected an intermittent single-tone DH type II burst starting at 23:55 UT at the frequency of 16 MHz. Also in this event the preceding type III burst intensified at 6 MHz and below, although type III emission is also visible at higher frequencies. The intensification of type III burst near 7 MHz is not as clear in this event as was in the previous two events and also the duration of the type III burst above frequencies of 6 MHz is longer than in the previous two events.

The 2013 May 22 event was associated with a M5.0 flare eruption at 12:58 UT at N15W70. The onset of this flare was overlapped by two preceding flares. The eruption was associated with a HCME observed 13:25 UT with an estimated space speed of 1702 km s^{-1}. Cheng et al. (2014) also studied the height of this flux rope eruption. They measured the

shock height to be 2.7 $R_{\odot}$ at 13:05 UT, which is consistent with our estimated height of 2.22 $R_{\odot}$ at the onset of the metric type II at 12:59 UT. Based on a 3-D flux rope fitting they estimated the maximum speed of the shock front to be around 1900 km s^{-1}, slightly higher than our estimated space speed. Their measurements also indicate that the CME reached the maximum speed about 5–10 minutes after the peak time of the X-ray flare, but the cadence of flux rope observations is 5–6 minutes. The type II burst started at 12:59 UT and again the type III burst visible in the Wind/WAVES dynamic spectrum show a clear intensification below 6 MHz. As was the case in the 2012 September 27 event the type III is visible above 6 MHz and the duration is longer than in the 2012 July 19 and August 31 events.

Both the 2012 July 19 and 2013 May 22 events had the flare onset obscured by a preceding flare, which explains why the flare-onset method underestimated the CME height. For the other two events on 2012 August 31 and September 27, the flare eruptions were isolated and the underestimation could not be due to erroneous onset time. We also looked at the time difference between the flare onset time and the type II onset time. The time differences for the four outliers are: 2012 July 19 (18 min), 2012 August 31 (10 min), 2012 September 27 (8 min) and 2013 May 22 (1 min). The mean (median) for the 59 events is 11 min (10 min). The range of the time differences is 1–39 min. Therefore, only the 2013 May 22 event corresponds to the extreme of the time range. In this case, the onset time of the flare could be too late, even though we have shifted it to 10 minutes earlier to 12:58 UT. The onset of the M5.0 flare is masked by two preceding flares. If we use the onset time of the first flare 12:30 UT, then the CME height at the type II onset will be 2.44 $R_{\odot}$. The 2012 July 19 event is marginally extreme. There are 11 events with a time difference larger than 18 min. Therefore, we conclude that the flare and type II onset times do not provide a good explanation for the underestimation of the CME height in the 2012 August 31 and September 27 events.

The other possibility is that the estimated space speeds of the CMEs, 1479 km s^{-1} and 1376 km s^{-1} respectively, were too low. Because the acceleration of the CME was assumed to be constant, doubling the final CME velocity doubles the distance CME travels in a fixed time period. However, in order to match the CME height of the flare-onset method with those of the spherical-shock we would need to multiply the space speed by factors 10.4 and 4.4 respectively. These correction factors obviously result in unrealistically high CME space speeds. Therefore, we conclude that the CME acceleration most likely deviated from the assumed constant acceleration that our simple model assumes.

The estimated space speeds of the five CMEs were in the range of 1358–1702 km s^{-1} with an average (median) speed of 1509 km s^{-1} (1479 km s^{-1}). The rest of the cycle-24 events had both lower (minimum 1120 km s^{-1}) and higher (maximum 3146 km s^{-1}) CME space speeds. The average (median) speed of all cycle-24 CMEs was 1793 km s^{-1} (1640 km s^{-1}). For the five events with the CME height over 2.0 $R_{\odot}$, the average and median space speeds are slightly less than those of all cycle-24 CMEs, but the CME speed variation is quite large. Therefore, the CME space speed cannot explain the higher CME height at the onset of the type II burst.

8. Complex Type III Bursts

The long-lasting or complex type III bursts have been found to be associated with SEP events (Cane et al. 2002; MacDowall et al. 2003). MacDowall et al. (2003) defined the complex type III bursts to be those with a duration of the radio burst at 1 MHz greater than or equal to 10 minutes. Gopalswamy et al. (2012b) found that all cycle-23 GLEs were associated with complex type III bursts. They estimated that all GLE-associated type III bursts had the 1 MHz duration greater than 20 minutes (average 32 min), except the type III burst associated with the GLE on 2005 January 17 that lasted 17 minutes. We also

estimated the type III duration at 1 MHz using WAVES/RAD2 data for all 59 events and found that all type III bursts lasted longer than 10 minutes. The type III associated with the 2003 June 17 SEP event had the shortest duration, 11 minutes. Therefore, the type III bursts in our study can be classified as complex type III bursts. However, one should note that Gopalswamy & Mäkelä (2010) found evidence that existence of a complex type III burst is not a sufficient condition for production of an SEP event.

Another issue related to the complex type III bursts is the reduced radio emission around 7 MHz observed in the Wind/WAVES dynamic spectrum (Reiner & Kaiser 1999). The 7 MHz corresponds to the height of $\sim$2.5 $R_\odot$ in the solar corona. Reiner & Kaiser (1999) suggested that the reduced type III emission is an indication of coronal region ($<$2.5 $R_\odot$) of disturbed magnetic fields that suppress type III emission either by preventing formation of well-defined electron beams or by reducing the directivity of the radio emissions via increased scattering and ducting. Gopalswamy (2004) suggests that this region of disturbed magnetic fields might be associated with a CME, because the complex type III bursts are also associated with fast and wide CMEs, which consist of large magnetic structures of high-density plasma. Therefore, CMEs could affect the propagation of electrons or radio emission, depending on the CME location with respect to the source of the electrons and the observer.

When we surveyed the 1–14 MHz type III radio emission measured by Wind/WAVES, we found that a clear lack of type III emission around 7 MHz and above was observable during cycle 23 in the 1998 April 20 (1.86 $R_\odot$), 2000 June 10 (1.79 $R_\odot$), 2000 October 16 (2.19 $R_\odot$), 2001 September 15 (1.91 $R_\odot$), 2002 January 14 (2.94 $R_\odot$) and 2002 March 22 (1.57 $R_\odot$) events and during cycle 24 in the 2010 August 14 (1.69 $R_\odot$), 2012 July 12 (2.01 $R_\odot$), 2012 July 19 (2.48 $R_\odot$), 2012 August 31 (2.29 $R_\odot$) and 2013 May 15 (1.87 $R_\odot$) events. The numbers in the parentheses are the shock heights at the onset of the metric type II

burst from Table 1. The cycle-24 heights are obtained by the spherical-shock method, which we expect to be more accurate. We only concentrate on events with a clear lack of type III emission, because in the WAVES observations around 10 MHz, the type III emission is occasionally masked by type II or type IV bursts. For the selected 11 events the shock formation heights range rom 1.57 $R_\odot$ to 2.94 $R_\odot$, while the average height is 2.05 $R_\odot$. The average shock height for all studied events (cycle-24 heights from spherical shock fit) is 1.79 $R_\odot$ and for the events without a clear lack of type III emission around 7 MHz it is 1.73 $R_\odot$. This apparent correlation between the lack of type III emission and the shock formation height at a higher range motivated us to examine the matter further.

Next we selected all events which had the estimated shock height at or above 2.00 $R_\odot$, which roughly corresponds frequencies below the upper limit of the Wind/WAVES observations at 14 MHz. There were a total of twelve events, i.e. another six events in addition to the six events with a clear lack of type III emission and the shock formation height at or above 2.0 $R_\odot$. Four events out of these new six events showed diminution of type III emission at or above 7 MHz, namely the 2002 April 17, 2002 April 21, 2003 June 17 and 2012 September 28 events. The two remaining events without a discernible diminution were the 2001 April 2 and 2001 October 22 events. These two exceptions had the estimated CME height of 3.61 $R_\odot$ and 2.39 $R_\odot$ respectively. The latter event has two flares closely overlapping, indicating that type III radio bursts could originate from two different sources. Therefore, observations during this event are inconclusive. The 2001 April 2 event was associated with the extremely intense, at least an X20 class, X-ray flare. Therefore, the extremely powerful flare might explain the intensity of the type III emission in this case. We also like to point out that the associated metric type II burst was analyzed by Mancuso & Abbo (2004). They found the metric type II burst to be complex and to exhibit clear evidence for a bifurcation of the radio emission lanes. They interpreted the emission to be due to interaction of the shock flank with a vertical current sheet.

If we compare the shock heights we estimated for non-GLE events with those of the cycle-23 GLE events estimated by Gopalswamy et al. (2012b), we notice that the average shock height at the onset of the metric type II burst for non-GLE events (1.79 $R_\odot$) is higher than that for GLE events (1.44 $R_\odot$). The estimated shock heights of the cycle-23 GLE events are in the range from 1.27 $R_\odot$ to 1.81 $R_\odot$. However, in the Wind/WAVES observations a possible diminution of type III emission around and above 7 MHz is seen during the GLE63 on 2001 December 26 (1.48 $R_\odot$) and GLE64 on 2002 August 24 (1.56 $R_\odot$). The numbers in parentheses are the estimated shock heights at the onset of the metric type II obtained from Table 1 in Gopalswamy et al. (2012b). The WAVES observations during the GLE64 are interrupted by a data gap that obscures the latter part of the complex type III burst, making it impossible to totally exclude the possibility of type III emission at frequencies above 7 MHz. The diminution during the GLE63 is better discernible, but partly overlapped by a DH type II burst. On the other hand, the estimated flare onset time of GLE63 is probably too late due to an overlapping preceding flare, therefore the shock height may be underestimated. However, both events have shock heights above the average of the GLE shock heights and close to the lower limit of the shock formation height range is 1.57–2.94 $R_\odot$ we obtained for the non-GLE events with a clear lack of type III emission.

Based on the above analysis, we suggest that our result supports the earlier interpretations (e.g., Reiner & Kaiser 1999; Gopalswamy 2004) that the CME/shock structure at the height of 2 $R_\odot$ or above may be connected to the diminution of type III emission around 7 MHz seen in complex type III bursts. However, a more extensive data set is required in order to infer how other factors, e.g. the relative locations of the source, the CME and the observer, contribute to the diminution of type III emission around and above 7 MHz.

9. Discussion

We studied the CME height at the onset of 59 metric type II radio bursts during cycles 23 and 24. We estimated the CME height by assuming that the CME onset occurs at the flare onset. As explained in Gopalswamy et al. (2012b), this assumption has sufficient observational and theoretical support: Yashiro et al. (2008) showed that flare sites predominately are located at the center of the CME span. Qiu et al. (2007) found a good correlation between the reconnection flux at the Sun and the flux of the associated magnetic cloud (CME) at 1 AU. Observational evidence also suggests that even the events without an observed flux rope structure at 1 AU could be flux ropes (e.g., Mäkelä et al. 2013). On the other hand in the standard theoretical model of solar eruptions known as the CSHKP model (Hanaoka et al. 1994), the flare and CME onsets are predicted to be simultaneous (Zhang et al. 2001).

Compared to the average CME height at the onset of type II burst during the GLE events (1.53 $R_\odot$; Gopalswamy et al. 2012b), we obtained for the non-GLE SEP events a slightly higher average (1.72 $R_\odot$). The most likely reason for the lower CME height at the type II onset during the GLEs event is that CMEs causing GLE events are faster than SEP-associated CMEs (Gopalswamy et al. 2010) and therefore probably accelerate more impulsively. For cycle-23 non-GLE SEP events, the average of initial acceleration (column 13 in Table 1) is +1.5 km s^{-2}. This is in good accordance with the result of Gopalswamy et al. (2012b) who found that the ratio of the initial acceleration of GLE-associated CMEs (+2.3 km s^{-2}) to ordinary CMEs (+1.0 km s^{-2}) was around two during cycle 23. Hence the mean initial acceleration of cycle-23 non-GLE SEP events is about half way between that of GLE-associated CMEs and ordinary CMEs. Recent studies also suggest that CME acceleration has a maximum around the time of the HXR peak of the associated flare (e.g., Temmer et al. 2008; Berkepile-Stoiser et al. 2012). Therefore, the GLE-associated CME is

able to drive the shock earlier at the lower height than during the non-GLE events.

Gopalswamy et al. (2013) estimated the heliocentric distance of CMEs at the onset of metric type II bursts from coronagraphic and EUV images of STEREO spacecraft that were observing in quadrature. They used both the wave-diameter and leading-edge methods and measured the CME heights for a set of 32 metric type II bursts from solar cycle 24. The shock heights were estimated using mainly a wave-diameter method, which assumes that the radius of the circle fitted to the outermost part of the EUV disturbance associated with the eruption corresponds to the shock height above the solar surface. They conclude that shocks form well below the height of 1.5 $R_\odot$. The CME height range extended from 1.20 to 1.93 $R_\odot$, only in a few cases the CME height was measured to be closer to 2 $R_\odot$. They found the mean shock height at the onset of the type II bursts to be 1.43 $R_\odot$, $\sim$17% lower than our result 1.72 $R_\odot$. Gopalswamy et al. (2013) did not check for an SEP association, but we found that most of the 32 events were not associated with an SEP event, only four events showed a minor SEP enhancement in the GOES >10 MeV channel. However, half (16) of the events had the heliographic longitude of the source region east of W20, making them less likely to be associated with a SEP event at Earth, because those events did not have a good magnetic connection to Earth. Because of the differences in the selection criteria and the estimation methods, it is difficult to make any firm comparisons between our results and those by Gopalswamy et al. (2013).

We found that the average (median) height varied between solar cycles: the cycle-23 average was 1.79 $R_\odot$ (1.61 $R_\odot$) while the cycle-24 average was 1.58 $R_\odot$ (1.45 $R_\odot$). However, statistical tests do not definitely reject the possibility of coincidence. Gopalswamy et al. (2009a) studied the CME images taken by STEREO/COR1 at the onset of type II bursts during the declining phase of solar cycle 23. They found that the average CME height to be around 1.5 $R_\odot$ which also is the distance at which the Alfvén speed profile has a minimum

value (e.g., Gopalswamy et al. 2001). This close correspondence of distances exists because the shock speed must be super-Alfvenic for it to accelerate particles. In addition, we know that the solar magnetic fields and density are weaker during the ongoing cycle 24 (e.g., Gopalswamy et al. 2014a). Gopalswamy et al. (2014a) found that for a given CME speed, the average CME width is higher for cycle-24 CMEs than for cycle-23 CMEs. This they explained as a consequence of the reduced total ambient pressure, including the reduced magnetic field. It is also possible that a given plasma density level corresponds to a lower radial height during cycle 24 than during cycle 23, explaining partly the lower average CME height at the type II onset in a manner described by Gopalswamy et al. (2009a). Therefore, we suggests that the difference in the average CME height between solar cycles 23 and 24 is due to a change in Alfvén speed profile between cycles 23 and 24.

We investigated also type III emission and found that out of 12 events with the estimated CME height at the type II onset at or above 2 $R_\odot$, only two events (2001 April 2 and 2001 October 22 events) did not show any clear evidence of diminution of type III emission above 7 MHz in the Wind/WAVES dynamic spectra. Reiner & Kaiser (1999) had noticed this feature when studying complex type III bursts. Our results support the suggestion that diminution of the type III bursts at and above 7 MHz, which corresponds to the coronal height of 2.5 $R_\odot$ is caused by the CME/shock structure at this height (Gopalswamy 2004).

10. Conclusions

We studied the CME height at the onset of 59 metric type II radio bursts that were associated with a major SEP event, excluding all GLE events, during solar cycles 23 and 24. We calculated the CME heights at the type II onset using a simple flare-onset method and found that the average CME height for non-GLE SEP events is ∼10% greater than

that for GLEs. We verified the results of the flare-onset method by comparing the results for cycle 24 non-GLE events with the results of the spherical-shock method. The correlation between the flare-onset and spherical-shock methods is reasonably good (CC=0.68). The discrepancies between the two methods are caused by errors in estimating the flare onset timing due to overlapping flares. The mean height (1.72 $R_\odot$) of the CME at the type II bursts onset for non-GLE SEP event was ~12% higher than that (1.53 $R_\odot$) for GLEs. The difference could be due to more impulsive acceleration of the GLE events. The mean initial acceleration of cycle-23 non-GLE SEP events is +1.5 km s^{-2}, about half way between that of GLE-associated CMEs (+2.3 km s^{-2}) and ordinary CMEs (+1.0 km s^{-2}) reported by Gopalswamy et al. (2012b). The mean CME height for cycle 23 non-GLE SEP events (1.79 $R_\odot$) is greater than for cycle 24 non-GLE SEP events (1.58 $R_\odot$), but statistical tests do not definitely reject the null hypothesis. The lower formation height of the shocks during cycle 24 could indicate a change in the Alfvén speed profile because of (a) the weaker solar magnetic fields and (b) plasma density levels closer to the surface than usual. We also found that complex type III bursts that showed diminution of type III emission in the frequency range of 7–14 MHz are more likely associated with events with large CME height at the type II onset (≥ 2 $R_\odot$), providing support for the suggestion that the CME/shock structure causes the feature.

REFERENCES

Bazilevskaya, G. A., Cliver, E. W., Kovaltsov, G. A. et al. 2014, Space Sci. Rev., published online, doi:10.1007/s11214-014-0084-0

Berkebile-Stoiser, S., Veronig, A. M., Bein, B. M., & Temmer, M. 2012, ApJ, 753, 88

Bougeret, J.-L., Kaiser, M. L., Kellogg, P. J. et al. 1995, Space Sci. Rev., 71, 5

Brueckner, G. E., Howard, R. A., Koomen, M. J. 1995, Sol. Phys., 162, 357

Cane, H. V., Erickson, W. C., & Prestage, N. P. 2002, J. Geophys. Res., 107, 1315

Cheng, X., Zhang, J., Olmedo, O. et al. 2012, ApJ, 745, L5

Cheng, X., Ding, M. D., Guo, y. et al. 2014, ApJ, 780, 28

Claßen, H. T. & Aurass, H. 2002, A&A, 384, 1098

Cliver, E. W., Nitta, N. V., Thompson, B. J., & Zhang, J. 2005, Sol. Phys., 225, 105

Delaboudinière, J.-P., Artzner, G. E., Brunaud, J. et al. 1995, Sol. Phys., 162, 291

Dorovskyy, V. V., Melnik, V. N., Konovalenko, A. A. et al. 2012, European Planetary Science Congress 2012 Abstracts, 7, EPSC2012-546

van Driel-Gesztelyi, L., Baker, D., Török, T. et al. 2014, ApJ, 788, 85

Gallagher, P., Lawrence, G. & Dennis, B. R. 2003 ApJ, 588, L53

Gibson, S. E., Foster, D., Burkepile, J., de Toma, G., & Stanger, A. 2006, ApJ, 641, 590

Gibson, S. E., Kucera, T. A., Rastawicki, D. et al. 2010, ApJ, 724, 1133

Gilbert, H. R., Inglis, A. R., Mays, M. L. et al. 2013, ApJ, 776, L12

Gopalswamy, N. 2003, Geophys. Res. Lett., 30, 8013

Gopalswamy, N. 2004, in Solar and Space Weather Radiophysics, ed. D. E. Gary & C. U. Keller, (Dordrecht: Kluwer Academic Publishers), 305

Gopalswamy, N. 2006, in Solar Eruptions and Energetic Particles, Geophys. Monogr. Ser. 165, ed. N. Gopalswamy, R. Mewaldt & J. Torsti, (Washington, DC: AGU), 207

Gopalswamy, N. & Mäkelä, P. 2010, ApJ, 721, L62

Gopalswamy, N. & Yashiro, S. 2011, ApJ, 736, L17

Gopalswamy, N., Kaiser, M. L., Thompson, B. J. et al. 2000, Geophys. Res. Lett., 27, 1427

Gopalswamy, N., Lara, A., Kaiser, M. L., & Bougeret, J.-L. 2001, J. Geophys. Res., 106, 25261

Gopalswamy, N., Thompson, W. T., Davila, J. M. et al. 2009a, Sol. Phys., 259, 227

Gopalswamy, N., Yashiro, S., Michalek, G. et al. 2009b, Earth Moon Planets, 104, 295

Gopalswamy, N., Xie, H., Yashiro, S., & Usoskin, I. 2010, Indian J. Radio Space Phys., 39, 240

Gopalswamy, N., Nitta, N., Akiyama, S., Mäkelä, P., & Yashiro, S. 2012a, ApJ, 744, 72

Gopalswamy, N., Xie, H., Yashiro, S. et al. 2012b, Space Sci. Rev., 171, 23

Gopalswamy, N., Xie, H., Mäkelä, P. et al. 2013, Adv. Space Res., 51, 1981

Gopalswamy, N., Akiyama, S., Yashiro, S. et al. 2014a, Geophys. Res. Lett., 41, 2673

Gopalswamy, N., Xie, H., Akiyama, S., Mäkelä, P., & Yashiro, S. 2014b, arXiv:1408.3617

Hanaoka, Y., Kurokawa, H., Enome, S. et al. 1994, Publ. Astron. Soc. Jpn, 46, 205

Howard, R. A., Moses, J. D., Vourlidas, A. et al. 2008, Space Sci. Rev., 136, 67

Inglis, A. R. & Gilbert, H. R. 2013, ApJ, 777, 30

Innes, D. E., Cameron, R. H., Fletcher, L., Inhester, B., & Solanki, S. K. 2012, A&A, 540, L10

Leblanc, Y., Dulk, G. A., & Bougeret, J.-L. 1998, Sol. Phys., 183, 165

Lemen, J. R., Title, A. M., Akin, D. J. et al. 2012, Sol. Phys., 275, 17

Li, T., Zhang, J., Yang, S., & Liu, W. 2012, ApJ, 746, 13

MacDowall, R. J., Lara, A., Manoharan, P. K. et al. 2003, Geophys. Res. Lett., 30, 8018

Mäkelä, P., Gopalswamy, N., Xie, H. et al. 2013, Sol. Phys., 284, 59

Mancuso, S. & Abbo, L. 2004, A&A, 415, L17

Mann H. B & Whitney D. R. 1947, Ann. Math. Stat., 18, 50

Nelson, G. J., Melrose, D. B. 1985, in Solar Radiophysics, ed. D. J. McLean & N. R. Labrum (Cambridge, New York: Cambridge University Press), 333

Qiu, J., Hu, Q., Howard, T. A., & Yurchyshyn, V. B. 2007, ApJ, 659, 758

Reiner, M. J. & Kaiser, M. L. 1999, Geophys. Res. Lett.26, 397

Saito, K., Poland, A. I., & Munro, R. H. 1977, Sol. Phys., 55, 121

Schmidt, J. M. & Cairns, I. H. 2014, J. Geophys. Res., 119, 69

Sheeley, N. R., Hakala, W. N., & Wang, Y.-M. 2000, J. Geophys. Res., 105, 5081

Temmer, M., Veronig, A. M., Vršnak, B. et al. 2008, ApJ, 673, L95

Thakur, N., Gopalswamy, N., Xie, H. et al. 2014, ApJ, 790, L13

Uchida, Y. 1960, Publ. Astron. Soc. Jpn, 12, 3

Vourlidas, A., Wu, S. T., Wang, A. H., Subramanian, P. & Howard, R. A. 2003, ApJ, 598, 1392

Vršnak, B. & Cliver, E. W. 2008, Sol. Phys., 253, 215, DOI 10.1007/s11207-008-9241-5

Wild, J. P. & McCready, L. L. 1950, Aust. J. Sci. Res. Ser. A, 3, 387

Williams, D. R., Baker, D., & van Driel-Gesztelyi, L. 2012, ApJ, 764, 165

Xie, H., Ofman, L., & Lawrence, G. 2004, J. Geophys. Res., 109, A03109

Yashiro, S., Gopalswamy, N., Michalek, G. et al. 2004, J. Geophys. Res., 109, A07105

Yashiro, S., Michalek, G., Akiyama, S., Gopalswamy, G., & Howard, R. A. 2008, ApJ, 673, 1174

Zhang, J., Dere, K. P., Howard, R. A., Kundu, M. R., & White, S. M. 2001, ApJ, 559, 452

Zhang, J. & Dere, K. P. 2006, ApJ, 649, 1100

Zucca, P., Carley, E. P., Bloomfield, D. S., & Gallagher, P. T. 2014, A&A, 564, A47

This manuscript was prepared with the AAS LATEX macros v5.2.
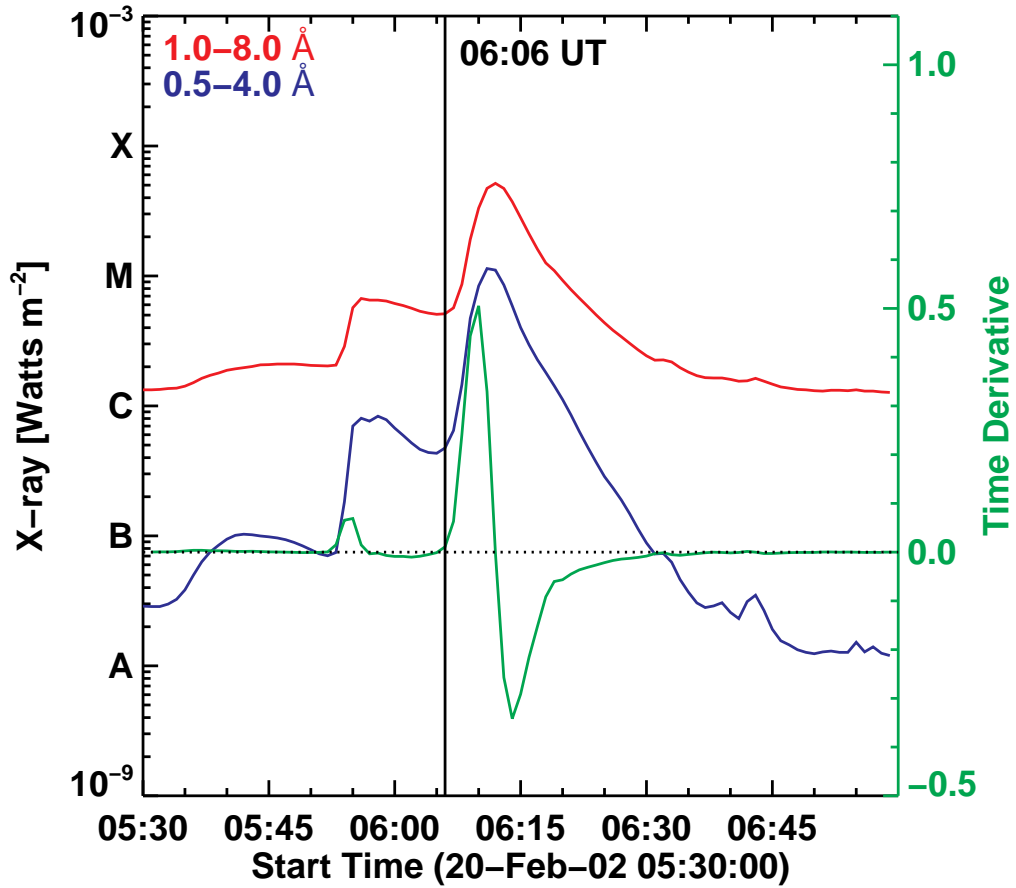
Fig. 1.— GOES soft X-ray light curves (red and blue lines) and the time derivative of the 1–8 Å curve (green line) during the 2002 February 20 event. The horizontal dotted line marks the zero value of the time derivative shown on the right Y-axis and the vertical line marks the revised onset time of the flare at 06:06 UT.
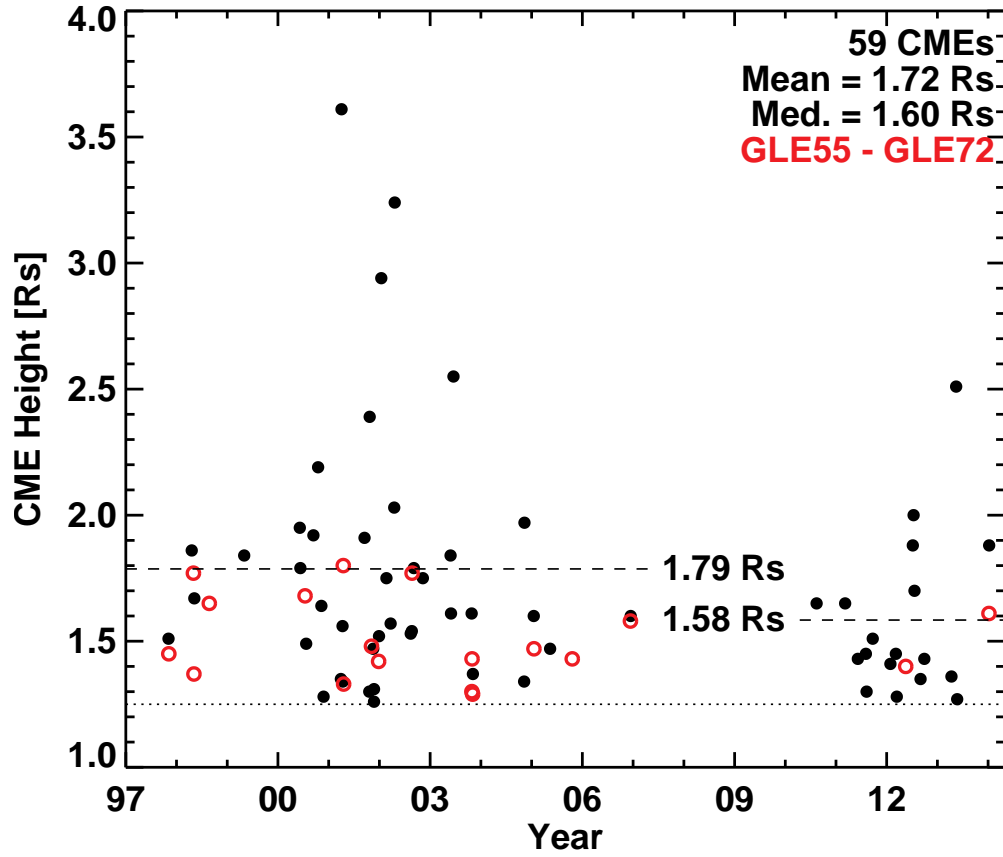
Fig. 2.— CME heights at the type II onset calculated using the flare-onset method. The horizontal dotted line marks the assumed CME starting height of $1.25\ R_\odot$. The CME heights at the type II onset for GLEs (including the 2014 January 6 event as a GLE72) are shown for comparison.
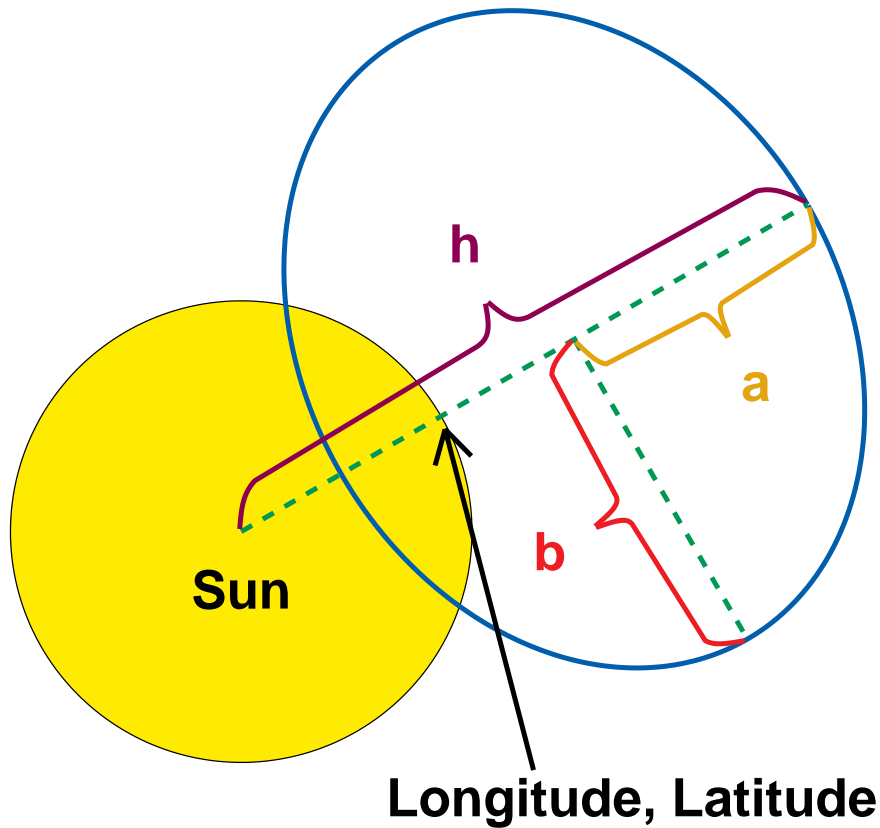
Fig. 3.— Schematic depiction of the 3-D shock model showing the definitions of the parameters. The five parameters used in fitting are: h=height, k=self-similarity coefficient, e=eccentricity, the longitude and latitude of the radial axis of the shock model on the solar surface. Because we were fitting a spherical shock, the eccentricity e was set equal to zero.
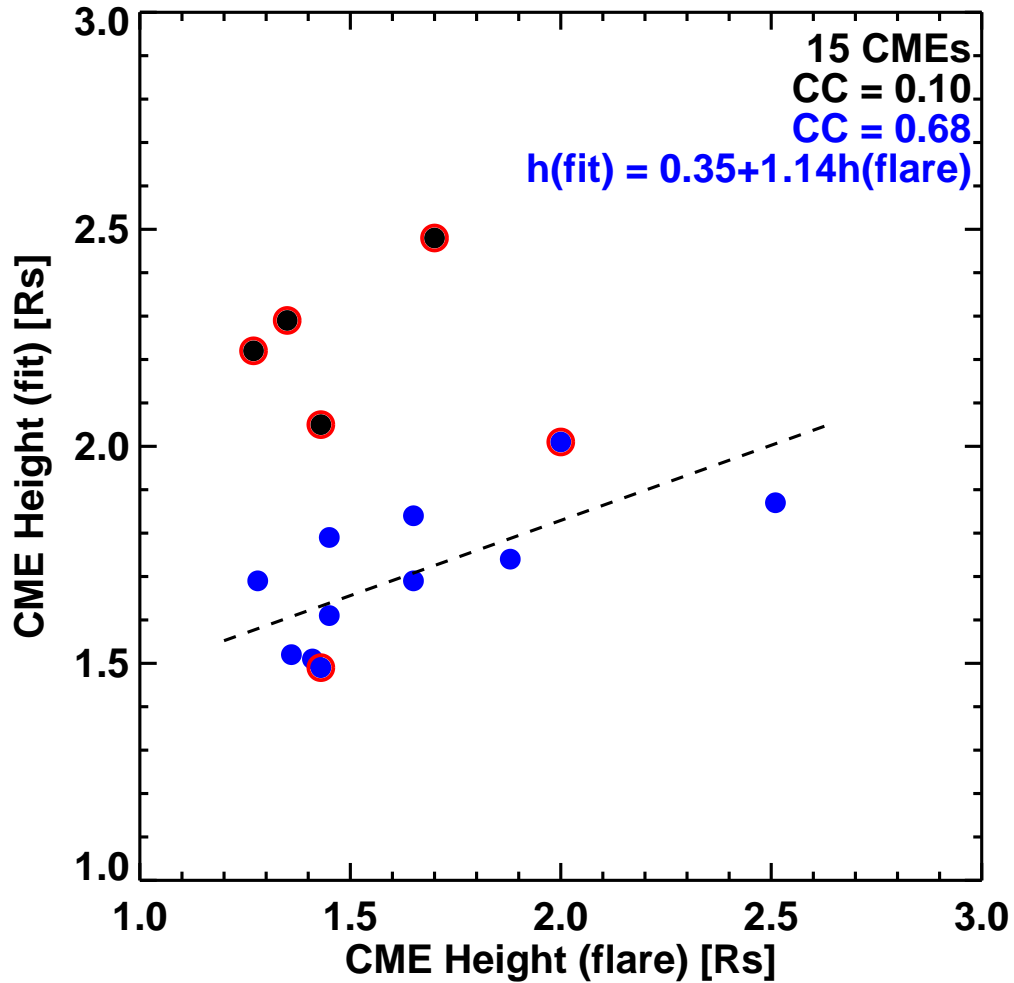
Fig. 4.— Comparison of CME heights at the onset of the type II bursts estimated using the flare-onset method and the spherical-shock method. The dashed line shows a linear fit to the 11 blue filled circles. The four outliers that were excluded from the fit are marked by black filled circles. Type II events that are listed to have a starting frequency below 160 MHz in the NOAA solar event report are marked by red circles. The equation of the regression line and the correlation coefficients for a data points including (black) and excluding (blue) outliers are plotted in the upper right corner.
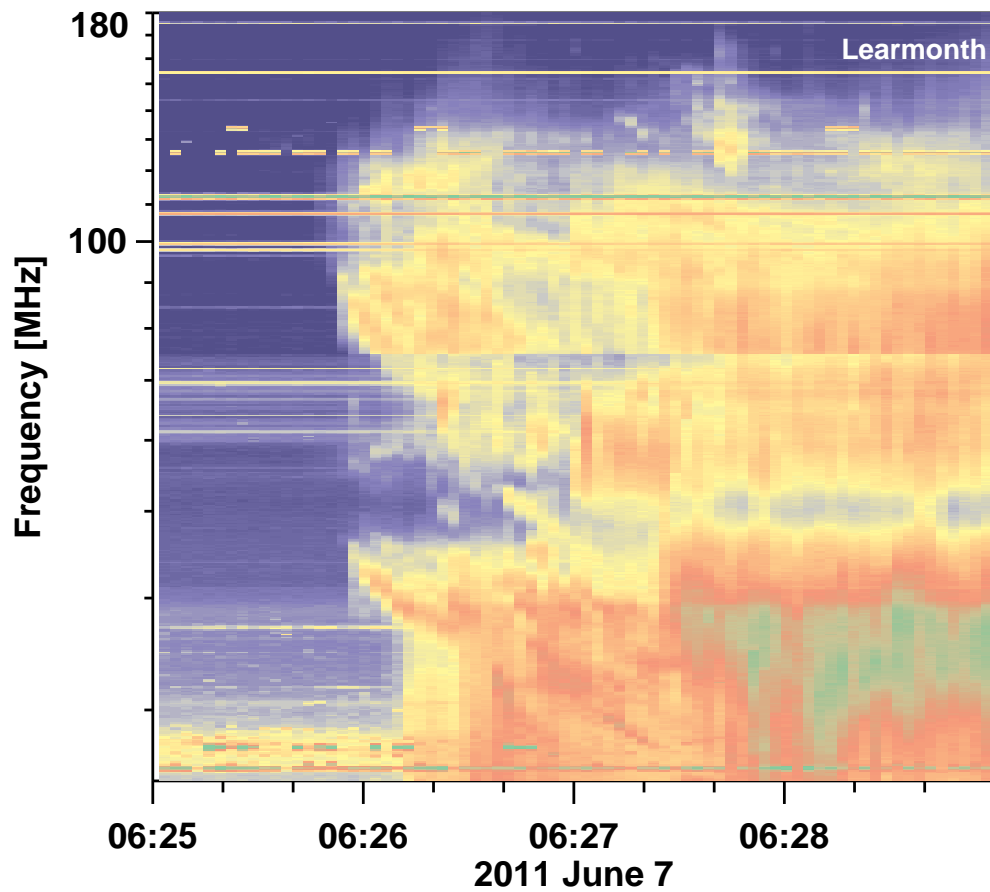
Fig. 5.— Dynamic spectrum of the onset of the 2011 June 7 radio burst observed by the Learmonth Solar Radio Spectrograph.

Table 1. Event Data

Type II Date & Time (UT)	CME Date & Time (UT)	Speed (km s⁻¹)	Width (deg)	Loc	Flare Onset Date & Time (UT)	Flare Peak Date & Time (UT)	Class	a4 (km s⁻²)	h4 (R⊙)	fit.h (R⊙)
1997/11/04 05:58	1997/11/04 06:10	993	360	S14W33	1997/11/04 05:52	1997/11/04 05:58	X2.1	2.76	1.51	–
1998/04/20 09:56	1998/04/20 10:07	1863	165	S43W90	1998/04/20 09:38	1998/04/20 10:21	M1.4	0.72	1.86	–
1998/05/09 03:26	1998/05/09 03:35	2331	178	S11W90	1998/05/09 03:16[a]	1998/05/09 03:40	M7.7	1.62	1.67	–
1999/05/03 05:50	1999/05/03 06:06	1824	360	N15E32	1999/05/03 05:36	1999/05/03 06:02	M4.4	1.17	1.84	–
2000/06/06 15:16	2000/06/06 15:54	1348	360	N20E18	2000/06/06 14:58	2000/06/06 15:25	X2.3	0.83	1.95	–
2000/06/10 16:55	2000/06/10 17:08	1228	360	N22W38	2000/06/10 16:40	2000/06/10 17:02	M5.2	0.93	1.79	–
2000/07/22 11:25	2000/07/22 11:54	1476	105	N14W56	2000/07/22 11:17	2000/07/22 11:34	M3.7	1.45	1.49	–
2000/09/12 11:43	2000/09/12 11:54	1946	360	S19W06	2000/09/12 11:23[a]	2000/09/12 12:13	M1.0	0.65	1.92	–
2000/10/16 07:08	2000/10/16 07:27	1336	360	N03W90	2000/10/16 06:40	2000/10/16 07:28	M2.5	0.46	2.19	–
2000/11/08 23:15	2000/11/08 23:06	1783	¿170	N10W77	2000/11/08 23:04[a]	2000/11/08 23:28	M7.4	1.24	1.64	–
2000/11/24 15:07	2000/11/24 15:30	1532	360	N22W07	2000/11/24 15:05[a]	2000/11/24 15:13	X2.3	3.19	1.28	–
2001/03/29 10:03	2001/03/29 10:26	1130	360	N20W19	2001/03/29 09:57	2001/03/29 10:15	X1.7	1.05	1.35	–
2001/04/02 21:52	2001/04/02 22:06	2609	244	N19W72	2001/04/02 21:32	2001/04/02 21:51	X20	2.29	3.61	–
2001/04/10 05:13	2001/04/10 05:30	2940	360	S23W09	2001/04/10 05:06	2001/04/10 05:26	X2.3	2.45	1.56	–
2001/04/12 10:18	2001/04/12 10:31	1294	360	S19W43	2001/04/12 10:13[a]	2001/04/12 10:28	X2.0	1.44	1.34	–
2001/09/15 11:29	2001/09/15 11:54	586	130	S21W49	2001/09/15 11:04	2001/09/15 11:28	M1.5	0.41	1.91	–
2001/10/19 16:24	2001/10/19 16:50	1051	360	N15W29	2001/10/19 16:21[a]	2001/10/19 16:30	X1.6	1.95	1.30	–
2001/10/22 14:53	2001/10/22 15:06	1603	360	S21E18	2001/10/22 14:27	2001/10/22 15:08	M6.7	0.65	2.39	–
2001/11/17 05:00	2001/11/17 05:30	1525	360	S13E42	2001/11/17 04:49	2001/11/17 05:25	M2.8	0.71	1.47	–
2001/11/22 20:22	2001/11/22 20:30	1472	360	S25W67	2001/11/22 20:18	2001/11/22 20:36	M3.8	1.36	1.31	–
2001/11/22 22:31	2001/11/22 23:30	1577	360	S17W36	2001/11/22 22:28[a]	2001/11/22 23:30	M9.9	0.42	1.26	–
2001/12/28 19:59	2001/12/28 20:30	2216	360	S24E90	2001/12/28 19:46[a]	2001/12/28 20:45	X3.4	0.63	1.52	–
2002/01/14 06:08	2002/01/14 05:35	1492	360	S28W90	2002/01/14 05:29	2002/01/14 06:27	M4.4	0.43	2.94	–

Table 1—Continued

Type II Date & Time (UT)		CME Date & Time (UT)		Speed (km s⁻¹)	Width (deg)	Loc	Flare Onset Date & Time (UT)		Flare Peak Date & Time (UT)		Class	a4 (km s⁻²)	h4 (R_☉)	fit.h (R_☉)
2002/02/20	06:15	2002/02/20	06:30	965	360	N12W72	2002/02/20	06:06[a]	2002/02/20	06:12	M5.1	2.68	1.75	–
2002/03/22	10:47	2002/03/22	11:06	1750	360	S10W90	2002/03/22	10:34[a]	2002/03/22	11:14	M1.6	0.73	1.57	–
2002/04/17	08:08	2002/04/17	08:26	1417	360	S14W34	2002/04/17	07:46	2002/04/17	08:24	M2.6	0.62	2.03	–
2002/04/21	01:19	2002/04/21	01:27	2422	241	S14W84	2002/04/21	00:43	2002/04/21	01:51	X1.5	0.59	3.24	–
2002/08/14	01:57	2002/08/14	02:30	1617	133	N09W54	2002/08/14	01:47	2002/08/14	02:12	M2.3	1.08	1.53	–
2002/08/22	01:55	2002/08/22	02:06	1034	360	S07W62	2002/08/22	01:47	2002/08/22	01:57	M5.4	1.72	1.54	–
2002/09/05	16:35	2002/09/05	16:54	2074	360	N09E28	2002/09/05	16:18	2002/09/05	17:06	C5.2	0.72	1.79	–
2002/11/09	13:17	2002/11/09	13:31	2159	360	S12W29	2002/11/09	13:08	2002/11/09	13:23	M4.6	2.40	1.75	–
2003/05/28	00:26	2003/05/28	00:50	1701	360	S07W20	2003/05/28	00:17	2003/05/28	00:27	X3.6	2.83	1.84[a]	–
2003/05/31	02:20	2003/05/31	02:30	1888	360	S07W65	2003/05/31	02:13	2003/05/31	02:24	M9.3	2.86	1.61	–
2003/06/17	22:48	2003/06/17	23:18	1918	360	S07E55	2003/06/17	22:27	2003/06/17	22:55	M6.8	1.14	2.55	–
2003/10/26	17:35	2003/10/26	17:54	2491	>171	N02W38	2003/10/26	17:21	2003/10/26	18:19	X1.2	0.72	1.61	–
2003/11/04	19:42	2003/11/04	19:54	2662	360	S19W83	2003/11/04	19:38[a]	2003/11/04	19:53	X28	2.96	1.37	–
2004/11/07	15:59	2004/11/07	16:54	2218	360	N09W17	2004/11/07	15:56[a]	2004/11/07	16:06	X2.0	3.70	1.34	–
2004/11/10	02:07	2004/11/10	02:26	3656	360	N09W49	2004/11/10	01:59	2004/11/10	02:13	X2.5	4.35	1.97	–
2005/01/15	22:34	2005/01/15	23:06	3682	360	N15W05	2005/01/15	22:25	2005/01/15	23:02	X2.6	1.66	1.60	–
2005/05/13	16:38	2005/05/13	17:12	2171	360	N12E11	2005/05/13	16:30[a]	2005/05/13	16:57	M8.0	1.34	1.47	–
2006/12/14	22:09	2006/12/14	22:30	1139	360	S06W46	2006/12/14	21:58[a]	2006/12/14	22:15	X1.5	1.12	1.60	–
2010/08/14	09:52	2010/08/14	10:12	1280	360	N17W52	2010/08/14	09:38	2010/08/14	10:05	C4.4	0.79	1.65	1.69
2011/03/07	19:54	2011/03/07	20:00	2223	360	N31W53	2011/03/07	19:43	2011/03/07	20:12	M3.7	1.28	1.65	1.84
2011/06/07	06:25	2011/06/07	06:49	1321	360	S21W54	2011/06/07	06:16	2011/06/07	06:41	M2.5	0.88	1.43	1.49
2011/08/04	03:54	2011/08/04	04:12	1477	360	N19W36	2011/08/04	03:49[a]	2011/08/04	03:57	M9.3	3.08	1.45	1.61
2011/08/09	08:01	2011/08/09	08:12	1640	360	N17W69	2011/08/09	07:59[a]	2011/08/09	08:05	X6.9	4.56	1.30	–

Table 1—Continued

Type II Date & Time (UT)		CME Date & Time (UT)		Speed (km s⁻¹)	Width (deg)	Loc	Flare Onset Date & Time (UT)		Flare Peak Date & Time (UT)		Class	a4 (km s⁻²)	h4 (R☉)	fit.h (R☉)
2011/09/22	10:39	2011/09/22	10:48	1905	360	N09E89	2011/09/22	10:29	2011/09/22	11:01	X1.4	0.99	1.51	–
2012/01/27	18:10	2012/01/27	18:27	2541	360	N27W71	2012/01/27	18:03[a]	2012/01/27	18:37	X1.7	1.25	1.41	1.51
2012/03/07	00:17	2012/03/07	00:24	3146	360	N17E27	2012/03/07	00:13[a]	2012/03/07	00:24	X5.4	4.77	1.45	1.79
2012/03/13	17:15	2012/03/13	17:36	1931	360	N17W66	2012/03/13	17:12	2012/03/13	17:41	M7.9	1.11	1.28	1.69
2012/07/06	23:09	2012/07/06	23:24	1611	360	S13E59	2012/07/06	23:01	2012/07/06	23:08	X1.1	3.84	1.88	1.74
2012/07/12	16:25	2012/07/12	16:48	1358	360	S15W01	2012/07/12	16:00[a]	2012/07/12	16:49	X1.4	0.46	2.00	2.01
2012/07/19	05:25	2012/07/19	05:24	1631	360	S13W88	2012/07/19	05:07[a]	2012/07/19	05:58	M7.7	0.53	1.70	2.48
2012/08/31	19:48	2012/08/31	20:00	1479	360	S19E42	2012/08/31	19:38[a]	2012/08/31	20:43	C8.4	0.38	1.35	2.29
2012/09/27	23:44	2012/09/28	00:12	1376	360	N06W34	2012/09/27	23:36	2012/09/27	23:57	C3.7	1.09	1.43[a]	2.05
2013/04/11	07:02	2013/04/11	07:24	1120	360	N09E12	2013/04/11	06:55	2013/04/11	07:16	M6.5	0.89	1.36	1.52
2013/05/15	01:37	2013/05/15	01:48	2127	360	N12E64	2013/05/15	01:16[a]	2013/05/15	01:48	X1.2	1.11	2.51	1.87
2013/05/22	12:59	2013/05/22	13:25	1702	360	N15W70	2013/05/22	12:58[a]	2013/05/22	13:32	M5.0	0.83	1.27	2.22
2014/01/07	18:17	2014/01/07	18:24	2410	360	S15W11	2014/01/07	18:04	2014/01/07	18:32	X1.2	1.42	1.88	–

[a]Flare onset time adjusted based on the logarithmic time derivative of the GOES soft X-ray flux.